Loss of ductility in optimized austenitic steel at moderate temperature: A multi-scale study of deformation mechanisms

Emilien Curtet, Bouzid Kedjar, Frédéric Mompiou, Hadi Bahsoun, Frédéric Pailloux, Arnaud Courcelle, Matthew Bono, Patrick Olier, Ludovic Thilly

Loss of Ductility in Optimized Austenitic Steel at Moderate Temperature: A Multi-scale Study of Deformation Mechanisms

Emilien Curtet[ab](emilien.curtet@cea.fr),
Bouzid Kedjar[b] (bouzid.kedjar@univ-poitiers.fr),
Frédéric Mompiou[c] (frederic.mompiou@cemes.fr),
Hadi Bahsoun[b] (hadi.bahsoun@univ-poitiers.fr),
Frédéric Pailloux[b] (frederic.pailloux@univ-poitiers.fr),
Arnaud Courcelle[d] (arnaud.courcelle@cea.fr),
Matthew Bono[d] (matthew.bono@cea.fr),
Patrick Olier[a] (patrick.olier@cea.fr),
Ludovic Thilly[b*] (ludovic.thilly@univ-poitiers.fr)

[a]DEN-Services de Recherches Métallurgiques Appliquées, CEA, Université Paris-Saclay, F-91191, Gif-sur-Yvette
[b]Institut Pprime, UPR 3346, CNRS, University of Poitiers, ISAE-ENSMA, SP2MI, Boulevard Marie et Pierre Curie, BP 30179, 86962 Futuroscope Chasseneuil Cedex, France
[c]CEMES, CNRS, Université de Toulouse, 29 rue Jeanne Marvig, 31055 Toulouse, France
[d]DEN-Service d'Etudes des Matériaux Irradiés, CEA, Université Paris-Saclay, F-91191, Gif-sur-Yvette
[*]Corresponding Author

Abstract

A Ti-stabilized cold-worked 15Cr-15Ni steel, called AIM1 (Austenitic Improved Material #1), has been selected as a candidate for the fuel cladding tubes of sodium-cooled fast reactors. This steel exhibits an unusual loss of ductility between 20 and 200°C for both solution-annealed and cold-worked conditions, which is similar to that observed for Twinning Indiced Plasticty steels and for the 200 and 300 series stainless steels. Therefore, a multi-scale study has been carried out to determine the deformation mechanisms that are active at different temperatures. Tensile tests have been performed to characterize the macroscopic material behavior, and Electron Backscattered Diffraction and Transmission Electron Microscopy characterization

techniques have been used to investigate the meso and micro-scale phenomena, such as the deformation microstructures and the evolution of the lattice defects. The parameters governing the deformation mechanisms have been examined, with particular attention paid to the conditions for mechanical twinning activation. This work required an original study of the variation of Stacking Fault Energy with temperature, based on the measurement of the dissociation extension of dislocation nodes. An increase in the SFE was observed between 20 and 200°C. After reviewing the existing models for predicting twinning, the present study proposes an approach based on the minimization of the total energy of the material to explain why twinning is not favorable at high temperatures. At 20°C, both dislocation slip and twinning are active and efficient mechanisms to release the strain energy. However, at 200°C, only dislocation slip is favorable and is often associated with dislocation cross-slip.

Keywords: Austenitic Steel, Tensile Properties, Mechanical Twinning, Cross-slip, Stacking Fault Energy.

1. Introduction

Austenitic stainless steels are excellent candidates for structural applications in many industrial sectors [1-2], because they exhibit a good combination of mechanical properties and corrosion resistance. In the nuclear industry, grades such as 316Ti or 15-15Ti were initially foreseen for fuel cladding tubes for sodium fast reactors [3–5]. These steels exhibit very little thermal creep, which allows them to withstand the pressure created by fission product release. In addition, recent alloys have relatively good resistance to irradiation swelling, and they can withstand up to about 130

Displacements Per Atom (DPA) without embrittlement [6]. In France, the Commissariat à l'Energie Atomique (CEA) developed the AIM1 (Austenitic Improved Material #1) austenitic stainless steel for the next generation of sodium-cooled fast reactors [7–10]. It is a Ti-stabilized, cold-worked 15Cr-15Ni steel, with the addition of minor elements such as carbon, silicon, phosphorus and boron.

Despite a high ductility over a large range of temperatures, AIM1 austenitic stainless steel exhibits an unusual behavior: unlike most metals, the tensile elongation exhibits a local minimum at 200°C , instead of continuously increasing with temperature [11]. At 200°C, the total elongation (TE) is reduced by a factor of 4 compared to that measured at 20°C. Fortunately, the elongation to failure increases at higher temperatures corresponding to the operating conditions of the reactor (400 to 650°C). Nonetheless, the origin of this singular tensile behavior must be understood if AIM1 is to be used as fuel cladding material.

A similar temperature dependence of tensile elongation to failure occurs in other steels, including several alloys optimized for nuclear environments [12–14] and more generally in all austenitic stainless steels of the 300 series [15-16] and the 200 series, where nickel is substituted with manganese for economic reasons [17]. A comparable behavior also occurs for Fe-Mn austenitic steels [18], which are mainly used for automotive applications. These materials have been largely studied and have been exhaustively reviewed by Bouaziz et al. [19] and De Cooman et al. [20].

The dependence of tensile elongation on temperature is believed to be directly related to the deformation mechanisms that are active at different temperatures. The large

elongation observed at low temperatures for the 200 and 300 series, Fe-Mn-C, and AIM1 austenitic steels is thought to be related to mechanical twinning, which is associated with the wide dissociation of perfect dislocations and the generation of large stacking faults. It has been shown that, for these steels, mechanical twinning occurs at low temperatures but not at high temperatures. Some authors suggest that the temperature dependence of the deformation mechanisms can be directly correlated to the Stacking Fault Energy (SFE or γ) values [21-22]. Others mention the existence of a so-called “twinning stress” which depends on the SFE [23]. It has been predicted that this twinning stress increases with temperature, and in fact it can exceed the ultimate tensile strength of the material [24], in which case, twinning will not occur anymore.

The current study proposes an original approach based on a multi-scale characterization of the deformation mechanisms and the exploration of the dependence of SFE on temperature for a 15Cr15Ni-Ti AIM1 austenitic stainless steel. At the macroscopic scale, tensile tests are performed on specimens made of AIM1 tubes at temperatures ranging from 20 to 600°C, to study the temperature dependence of the elongation to failure. At the mesoscopic scale, post-mortem characterizations of the tensile specimens by Electron Backscattered Diffraction (EBSD) and by Transmission Electronic Microscopy (TEM) are performed to identify the temperature ranges at which the different deformation mechanisms occur. At the microscopic scale, in-situ TEM tensile tests are used to study the nature of the lattice defects involved in the deformation mechanisms. Additional in-situ TEM heating tests are carried out to measure the SFE using the extended node method at temperatures

ranging from 20 to 500°C. In light of the obtained results and the existing models, a discussion is conducted to explain the loss of ductility of the 15Cr15Ni-Ti AIM1 austenitic stainless steel at 200°C.

2. Materials and experimental procedures

2.1 Materials

The steel used for this study was taken from a cast of about 6 tons produced by Aubert & Duval using induction melting followed by vacuum arc remelting [7]. Primary shapes obtained by hot forging enabled the production of two different geometries: cladding tubes resulting from an industrial route involving several processes with intermediate annealing (i.e. hot extrusion, cold pilgering and several passes of cold drawing), and fine sheets produced at the laboratory scale using hot and cold rolling and intermediate annealing.

The cladding tubes have an external diameter of 9.70 mm and a wall thickness of 0.50 mm. The final step of the manufacturing process is a cold drawing with 20% cold-work. Tubes are studied both in this as-received cold-worked condition (T-CW), and after solution annealing at 1130°C in an argon atmosphere (T-SA). The 1.3-mm-thick sheets are studied after a solution annealing at 1130°C under vacuum (S-SA). For each condition, the grain size measured in the transverse direction is similar with a G value of 7-8 according to the NF EN ISO 643 (corresponding to a mean grain diameter of 20-30 µm).

The chemical composition of the ingot was measured by the supplier. The main alloying elements are presented in Table 1.

2.2 Tensile Tests and post-mortem characterizations

Tensile specimens are machined from AIM1 tubes using electrical discharge machining. The specimens have a “two-leg” geometry, as shown in Figure 1(a), with a nominal gauge length of 30 mm and a cross section of 3.06 mm². The tests are conducted on a screw driven INSTRON 8862 machine at a nominal strain rate of 3.10^{-4} s^{-1} (quasi-static loading conditions) at temperatures ranging from 20 to 600°C. The applied force is measured with a 100 kN load cell. The applied axial strain is continuously measured using a high temperature MAYTEC extensometer with ceramic sensor arms. Once necking occurs, the elongation of the sample is measured using the displacement of the cross head.

Post-mortem examinations are conducted on the specimens using EBSD and TEM analyses. After the tensile tests, several specimens are embedded in a conductive resin and mechanically ground to a mirror-polish, to ensure the tensile direction would be normal to the scanned surface. The hardened layer is removed by 6 hours of vibratory polishing in an OPS solution. High-resolution EBSD maps are collected with a step size of 25 nm in a Helios Nanolab G3 CX Dual Beam Field Emission Gun (FEG) - SEM from ThermoFisher equipped with a high sensitivity HIKARI Super EBSD camera from EDAX. The maps are acquired with the TEAM software and processed with the OIM 7 software. Crystal orientation maps are displayed as inverse pole figures (IPF) maps. The image quality (IQ) is overlaid on each IPF map, which reveals the non-indexed pixels associated to grain and twin boundaries. After EBSD analysis, specific areas are selected for thin foil extractions with the Focused Ion Beam (FIB) using the standard

lift-out method [25]. Subsequently, the TEM observations are performed on a JEOL 3010 operating at 300 kV.

2.3 In-situ TEM tensile tests

Tensile specimens for in-situ TEM straining experiments are machined from the solution annealed AIM1 sheet (S-SA). They are mechanically ground to less than 100 µm thickness and milled to the shape of tensile specimens. The center of the gauge section is electrolytically twin-jet polished with a Struers Tenupol 5 in an electrolytic solution composed of 10% perchloric acid and 90% ethanol at -10°C (see Figure 1(b)). The in-situ tensile tests are conducted using a custom-made high-temperature straining holder (more details are presented in [26]) in a JEOL 2010HC microscope operating at 200 kV. The experiment consists of applying an incremental displacement while monitoring the dynamical response during stress relaxation. Dislocation motions are video recorded at 25 fps using a MEGAVIEW III camera. In all the displayed micrographs, the sample holder axis, which also corresponds to the straining direction, is vertical. Electron diffraction is used in order to determine the grain orientations [27].

2.4 Measurement of the Stacking Fault Energy

Several methods exist to determine the SFE using direct TEM observations of dislocation configurations, as reviewed by Ruff [28]. Two of the more accurate techniques are the “extended dislocation node” method and the “isolated dislocation” approach. The isolated dislocation approach is the more recent method and is recommended by many researchers [29–31] but, to our knowledge, it has not been used to examine variations of SFE as a function of temperature. In contrast, the

extended dislocation node method has been widely used to determine the temperature dependence of SFE in many types of close-packed metals, as discussed in the review by Rémy et al. [32]. An example of an extended dislocation node under different observation conditions in S-SA at 20°C is presented in Figure 2.

The extended dislocation node method was initially proposed by Whelan [33] and then improved by Brown and Thölen [34]. It is based on the calculation of the self-stress of a dislocation. In this theory, each branch of the node is divided into several straight segments that interact with each other, with the stacking fault in the center. There is an equilibrium configuration that depends on the material properties, including the SFE. The estimation of the SFE, γ, is based on the measurement of the inner node radius and the curvature of the dislocation, as given by equation (1):

$$\gamma = \frac{\mu {b_p}^2}{y}\left\{0.055\left(\frac{2-\upsilon}{1-\upsilon}\right) - 0{,}06\left(\frac{\upsilon}{1-\upsilon^2}\right)cos2\alpha + \left[0.018\left(\frac{2-\upsilon}{1-\upsilon}\right) + 0.036\left(\frac{\upsilon}{1-\upsilon}\right)cos2\alpha\right] log_{10}\frac{R}{b_p}\right\} \quad (1)$$

Where μ is the shear modulus, υ is the Poisson's ratio, α is the angle between the dislocation lines and the Burgers vectors, and b_p is the magnitude of the partial Burgers vector. R is the curvature of the dislocation and y is the inner node radius, as illustrated in Figure 2(b).

μ and υ are determined by acoustic methods on AIM1 at 20°C. Their values are respectively 80 GPa and 0.28. The variations of μ and υ with temperature are extrapolated from data available for 316 austenitic stainless steel [35], which has a composition similar to AIM1. For AIM1, b_p is equal to 0.146 nm.

To determine α, the Burgers vectors of the partial dislocations must be identified. Figure 2(a) presents a series of extinction conditions for each partial dislocation, which allow for their Burgers vectors to be determined. In Figure 2(c), the dislocation line, the Burgers vector direction, and the Burgers vector components are drawn with a unique color for each partial dislocation. α is the angle between the Burgers vector direction and the tangent to the dislocation line, as shown in Figure 2(d). Here, it is always equal to 30°.

If the electron beam is not orthogonal to the plane containing the node, then the node image is subjected to projection distortions that affect the apparent value of y. To account for this effect, Tisone et al. [36] suggested measuring the perimeter P_w of an equilateral triangle inscribed within the inner circle of the projected node, as shown in Figure 2(e). Then, the true value of y, y_t, can be determined with using equation (2) :

$$y_t = \frac{P_w}{\sqrt{3}\,[1+\sqrt{1+3cos^2(\psi)}]} \quad (2)$$

Where ψ is the angle between the normal to the plane of the node and the electron beam.

Given that $P_w = 3\sqrt{3}y$, a correction factor can be established between the projected value of y, y_p, and y_t, as defined by equation (3):

$$y_t = \frac{3}{1+\sqrt{1+3cos^2(\psi)}} y_p \quad (3)$$

The examinations in this study are performed on a JEOL 2200-FS operating at 200 kV. The sample is heated with a commercial single-tilt holder (model 628Ta from Gatan).

3. Results

3.1 Mechanical results

The results of the tensile tests obtained on tubes are shown in Figure 3. The engineering stress-strain curves of T-CW and of T-SA are plotted respectively in Figure 3(a) and Figure 3(b) for five different temperatures. The 0.2% offset Yield Stress (YS), the Ultimate Tensile Stress (UTS) associated with uniform elongation (UE), and the total elongation at fracture (TE) as a function of test temperature are shown in Figure 3(c) for T-CW and in Figure 3(d) for T-SA.

By comparing Figure 3(a) and (b), it appears that the solution annealing significantly increases the elongation over the temperature range from 20 to 600°C. For both conditions (CW and SA), the best properties (elevated UE, TE, YS, UTS) are obtained at 20°C. In addition, Figure 3(d) shows that the UTS values for T-SA are approximately three times the YS values. Figure 3(c) indicates that cold-work significantly enhances the YS but only slightly increases the UTS. For both conditions (CW and SA), the UTS and YS decrease as the temperature increases, and the lowest strength values are obtained at 600°C. However, elongation to failure decreases as the temperature increases from 20 to 200°C, with the uniform elongation dropping drastically by a factor of 10 for T-CW and by a factor of only 1.5 for T-SA. The lowest TE is measured at 200°C for T-CW (TE ~ 3%) and 500°C (TE ~ 31%) for T-SA.

3.2 Microstructural results

3.2.1 Post mortem EBSD observations

The high-resolution EBSD technique provides detailed views of the microstructure at the mesoscopic scale. Figure 4(a) represents the initial CW state, in which the grains are plastically deformed and the crystallographic lattice is distorted, as shown by the color gradients. These images indicate that the mechanism of dislocation glide and storage is active during the cold-working of the tubes. Mechanical twinning is also active, and both isolated twins and intersecting twin systems are evident in many grains. Many of the twins are too thin to be indexed, but they are identifiable by dark lines since the presence of the nano-twins locally degrades the quality of the indexing as transcribed in Index Quality, IQ.

Figure 4(b) shows the effects of a uniaxial tensile test at 20°C on the cold-worked state with a homogenous deformation of about 10%. The additional deformation of 10% has clearly increased the number and width of the twins compared to the CW state shown in Figure 4(a). The color gradients are also more pronounced, which means that dislocation glide remains active.

Figure 4(c) shows the effects of a uniaxial tensile test at 200°C on the cold-worked state with a homogenous deformation of about 1%. The IPF map does not reveal any significant changes in the microstructure after this test compared to the initial state.

Figure 4(d) illustrates the microstructural transformations caused by a solution annealing heat treatment. The grains are defect-free, and only very large annealing twins are observed.

Figure 4(e) and (f) show the effects of uniaxial tensile tests at 20°C on the solution annealed state with a homogenous deformation of about 45% (e), and at 200°C with a homogenous deformation of about 30% (f). Dislocation glide and storage are observed in both cases, while mechanical twinning is only present at 20°C (e) and not at 200°C (f).

With the exception of the initial T-SA (Figure 4(d)), two grain families emerge on the IPF maps: one called “type I” grains with the <001> directions aligned to the tensile direction (color close to red) and the other one called “type II” grains with the <111> directions aligned to the tensile direction (color close to blue). It is worth mentioning that for T-CW tested at 20°C, the mechanical twins are uniformly and indifferently distributed throughout all the grains (types I and II), while for T-SA tensile tested at 20°C, they are seen only in type II grains.

In Figure 4(b) and (c), it is difficult to distinguish between twins that may have formed during cold-working or during the tensile test. Consequently, the next step of the study focuses on the solution annealed state, which does not contain any mechanical twins prior to the tensile tests.

The features seen on EBSD maps strongly depend on the resolution of the images. In particular, despite choosing the smallest possible step (here 25 nm), it is possible that very thin nano-twins could be present but not detected. To confirm the presence or absence of nano-twins in some grains, it is necessary to reduce the scale of observation from mesoscopic to microscopic using TEM observations.

3.2.2 Post mortem TEM observations

Figure 5 presents TEM micrographs obtained on SA samples after tensile tests up to maximum UE at 20°C and 200°C. Areas of interest were selected from IPF maps, and targeted extractions of thin foils were performed by FIB milling via the lift-out technique. At each temperature, the thin foils were extracted in both type I and II grains.

Mechanical twins are clearly visible in the type II grain after deformation at 20°C (image (5b)), while none can be seen in the type I grain on micrograph (5a). No twins are evident in any of the grains deformed at 200°C for either orientation (micrographs (5c) and (5d)).

The TEM observations provide additional details that are not seen in the EBSD maps. Some of the twins in Figure 5(b) do not exceed 50 nm in thickness and are arranged in bundles of a few hundred nanometers, which suggests that some of the twins observed by EBSD may actually be bundles of very thin twins that cannot be individually resolved at the used resolution. Likewise, it is difficult to distinguish different twinning systems with EBSD maps. However, on TEM micrograph (5b), the existence of primary (labelled T1) and secondary (labelled T2) twinning systems is evident, where the T2 system has formed in regions of the matrix bounded by T1.

It is interesting to note that well-defined dislocation cells are visible in Figure 5(c) and (d) for the grains deformed at 200°C. In contrast, only a slight tendency for dislocation cells is observed for the grains deformed at 20°C in Figure 5(a).

3.3 In situ TEM straining experiments

In-situ TEM experiments are carried out at 20°C and 200°C on S-SA. Figure 6 shows images extracted from a video recorded at 20°C. The sequence describes the formation of a stacking fault and its evolution. The images are acquired in two-beam conditions with $\vec{g}$= (002). The observed area is in the middle of a grain, which is strained along a direction <032>. At the beginning of the sequence in Figure 6(a), two bands with dark fringes corresponding to stacking faults (labelled (i)) are clearly visible. These stacking faults were present prior to the straining and remain stable for the duration of the sequence; their habit plane is (111). Upon straining, a perfect dislocation, labeled (ii) in Figure 6(b), glides on a $(1\bar{1}\bar{1})$ plane through the grain until it is pinned on the upper stacking fault. The perfect dislocation leaves two dark slip traces corresponding to a step left at the intersection between the $(1\bar{1}\bar{1})$ plane and the foil surfaces. As the deformation continues, a leading partial dislocation is emitted from this pinning point, and a new stacking fault is generated in the $(1\bar{1}\bar{1})$ plane (labeled (iii) in Figure 6(c)). A breakaway of the leading partial then occurs (labeled (iv) in Figure 6(d)).

In Figure 6(e), the stacking fault abruptly disappears (although the observation conditions are unchanged), leaving behind only slip traces (labeled (v)). It is thus likely that the trailing partial dislocation was emitted at the pinning point, erasing the fault induced by the leading partial dislocation.

The sequence presented in Figure 7 is extracted from observations at 200°C. In this sequence, the stress direction is aligned with a direction <133> of the crystal. The

conditions correspond to a two-beam observation with $\vec{g}$= (002). The dissociation of dislocations and the nucleation of stacking faults are not observed at this temperature. Rather, perfect dislocations glide in the same plane (probably nucleated from a single dislocation source) and cross-slip occurs occasionally. It must be emphasized that the velocity of dislocations is extremely high, and it is difficult to fully capture dislocation movements. Figure 7(a) exhibits two slip traces on a $(\bar{1}\bar{1}1)$ habit plane, left by previous dislocation displacements (labeled (i)). In Figure 7(b), a dislocation initially glides in the $(\bar{1}\bar{1}1)$ plane but suddenly cross-slips into the adjacent $(1\bar{1}\bar{1})$ plane (labeled (ii)). Thereafter, the dislocation stops moving and can be clearly seen (segment (iii)).

3.4 Temperature dependence of the Stacking Fault Energy

SFE measurements are carried out between 20 and 500°C in S-SA. Figure 8 exhibits the evolution of an extended dislocation node at different temperatures. As was the case for Figure 6 and Figure 7, the observation conditions are two-beam with $\vec{g}$= (002), which offer the best contrast. The tilt is maintained at 0° to keep the thickness of the foil as small as possible. In this case, the angle ψ is equal to 50°. The correction factor given by equation (3) is equal to 1.2.

The sequence in Figure 8 clearly shows that the node constricts as the temperature increases from 20 to 500°C. At 400 and 500°C, the extension of the node becomes so small that it is difficult to measure it with reasonable uncertainty, at the observation resolution.

The parameters necessary for estimating the SFE at each temperature, using equation (1), are listed in Table 2. The calculated values of SFE (γ and the associated uncertainty ($\Delta\gamma$) (taking into account (Δy) and (ΔR)) are given in the last two columns.

The node sizes, and thus the calculated SFE values, increase almost linearly with temperature over the range 20 to 300°C, as shown in Figure 9. The calculated SFE appears to stabilize at approximately 60 mJ/m over the range 300 to 500°C. However, because the uncertainty is rather large at 400°C and 500°C, further analysis will concentrate on the SFE values in the 20-300°C temperature range.

4 Discussion

4.1 SFE values and their variation with temperature in AIM1 austenitic stainless steel

SFE values measured by previous researchers on steels with a composition close to 15 wt% chromium and 15 wt% nickel at temperatures near 20°C have been compiled by Meric de Bellefon et al. [37]. The values are generally between 22 and 30 mJ/mm². The reported SFE of DIN 1.4970 steel, which has a very similar chemical composition to AIM1, is 30 mJ/mm² at 20°C [38]. Thus, the value of 27 mJ/mm² for AIM1 measured at 20°C in the present study is consistent with previously measured values on similar steels.

Since there is no reported data above 20°C for compositions near 15 wt% chromium and 15 wt% nickel, the present results are compared to other ternary Fe-Ni-Cr systems, which have been reviewed by Remy et al. [32]. In the present study, the SFE is calculated using the extended dislocation node method, which is based on the calculation of the self-stress of a dislocation. According to Latanision et al. [39], SFE

calculations using this method are reliable up to 325°C. In fact, reversible changes in the node size have been observed from 20°C to 325°C for 11Ni-18Cr and 16Ni-19Cr steels. Moreover, above 325°C, aging effects appear, like the formation of solute atom atmospheres, and may impede the movement of partial dislocations. Such effects may affect the size of the node in addition to the sole self-stress of the dislocations. We also recall that the calculated SFE values become less accurate above 300°C. Therefore, at 400°C and 500°C, it is difficult to speculate on the accuracy of the SFE values presented in Table 2 and in Figure 9. These values thus appear in parentheses in the table and in red on the graph, and they are presented for reference only.

A linear regression through the SFE values measured in this study in the temperature range of 20 to 300°C has a slope, $d\gamma/dT$, of 0.09 ± 0.02 mJ/m²/°C. This value is in good agreement with values found in the literature [32]. Lecroisey et al. found a slope, $d\gamma/dT$, of 0.08 mJ/m²/°C at room temperature for steels with a composition range between 7-18 wt% chromium and 11-20 wt% nickel [40]. Abrassart found a slope, $d\gamma/dT$, of 0.1 mJ/m²/°C for a Fe-18Cr-7Ni-0.18C steel in the temperature range 20-330°C [41].

4.2 Overview of the reported deformation mechanisms of austenitic stainless steels

It is well known that some metallic alloys exhibit a reduction in elongation to failure when Dynamic Strain Aging (DSA) occurs. Hong et al. confirmed that DSA plays a role in the ductility of 316L steel, but only for temperatures between 250°C and 600°C [42]. Thus, it is unlikely that DSA can explain the reduction in elongation of AIM1 between 20°C and 200°C.

Another hypothesis is that the reduction in elongation may be related to twinning. As explained above, the following trends were identified in the current study :

- At 20°C, the dominant deformation mechanisms are twinning and perfect slip.
- At 200°C, the dominant deformation mechanism is perfect slip associated with cross-slip.

This has been confirmed by Michel et al. [43] that performed tensile-tests and examined the deformation microstructures at UE on 316 steel. The occurrence of two intersecting twinning systems is observed by TEM at 21°C, while only cells with walls composed of massive dislocation tangles are observed at 204°C. In the same condition of mechanical testing on 316L, Wu et al. [24] observed by EBSD a large presence of twins at 20°C, but they did not observe any at 200°C. Furthermore, Byun et al. [44] identified, after a strain about 15% by disk-bend deformation on 316LN, large stacking faults at 20°C and tangled dislocations at 200°C.

In the existing literature, only a few studies have tried to explain the temperature dependence of the deformation mechanisms for austenitic stainless steels. They have been reviewed by Meric de Bellefon [45].

For a 316LN steel, Byun et al. [44] suggest that the deformation mechanisms are governed by the applied stress. At stresses lower than 400 MPa, dislocation tangles are dominant and between 400 and 600 MPa, the first stacking faults are formed. In this scenario, at least 600 MPa is required for massive twinning to be possible. Since 600 MPa is never achieved during tensile tests at temperatures greater than 200°C for 316LN steel, twinning does not occur at these temperatures.

Other studies propose the existence of a critical stress for twinning σ_T [23], which is supposed to be proportional to the SFE as detailed in equation (4):

$$\sigma_T = \frac{2}{SF}\frac{\gamma}{b_p} \quad (4)$$

where γ and b_p are the SFE and the magnitude of the partial Burgers vector, and SF is the average Schmid factor. Byun suggests a proportionality coefficient of $\frac{2}{SF} = 6.14$ for a 316 steel [23].

In the case of AIM1 steel, using a similar proportionality coefficient of $\frac{2}{SF} = 6.14$ and a SFE value of 27 mJ/m² at 20°C (as measured in the present study), equation (4) leads to a critical stress for twinning σ_T of 1135 MPa. This value exceeds the UTS of AIM1 at 20°C (true stress of about 830 MPa). Thus the calculation indicates that twins cannot form in AIM1 at 20°C, which is clearly not the case.

One plausible origin of this discrepancy is the potential difference between the macroscopic applied stress and the local three-dimensional stress seen by the grains, related to their individual crystallographic orientation and the geometric constraints imposed by their neighboring grains. Because the local stress can greatly exceed the macroscopic stress and is very difficult to determine for a polycrystalline material, the prediction of twinning based on a critical stress is often not straightforward.

Other authors explain the temperature dependence of the deformation mechanisms not in terms of stress but in terms of SFE evolution. Some authors have reported that twinning can be active only in a narrow range of SFE values between 20 and 35-40 mJ/m² [21,22,46–49]. Above 35-40 mJ/m², dislocations are rarely dissociated and slip of non-dissociated perfect dislocations is favored. These findings are consistent with

the results obtained in the present study: twinning is only observed when the SFE of AIM1 stainless steel is around 27 mJ/m² and is not observed when it reaches values larger than 40 mJ/m². However, a low SFE value is a necessary but not sufficient condition for twinning to occur [50].

4.3 Competition of the deformation mechanisms of AIM1 austenitic stainless steel

In addition to the aforementioned discussion of the temperature dependence of the deformation mechanisms in terms of SFE , it should be recalled that the driving force for the plastic deformation of the material is the strain energy that is produced during the tensile test. The material always chooses the most energetically favorable mechanism for relieving the accumulated strain energy, and the most energetically favorable mechanism is a function of the temperature.

The events occurring during the in-situ TEM video sequence presented in Figure 6 can be explained using this approach. Figure 6 initially shows a dislocation that glides freely until it encounters a preexisting stacking fault that impedes its movement. At this point, the dislocation has several options. It can simply stop moving, or cross slip into a different plane, or dissociate into partial dislocations. At 20°C, cross slip requires a large amount of energy, so the dislocation is unable to use this mechanism to overcome the obstacle. Because the glide of the dislocation is arrested while the sample continues to be strained, the strain energy increases and becomes so large that it exceeds the relatively low SFE. Thus, it becomes energetically favorable for the dislocation to dissociate and form a stacking fault, as shown in Figure 6(c).

The SFE values presented in Table 2 indicate the level of strain energy required to form twins at a given temperature. A stacking fault will only form if it requires less energy than the other mechanisms available.

In AIM1 stainless steel, γ is only 27 mJ/m² at 20°C, so dislocations can dissociate and twins can form when the strain energy reaches this value. However, as the temperature increases to 200°C, γ increases to 46 mJ/m². At this temperature, the energy required to cross-slip is lower than that required to form a twin. So, cross-slip becomes the most efficient mechanism for releasing the strain energy, and therefore twinning is rare.

Thus, once the majority of the perfect dislocations become obstructed and cannot glide freely, the deformation mechanisms of AIM1 austenitic stainless steel become governed by a competition between twinning and cross-slip for releasing the strain energy.

4.4 Effect of deformation mechanisms on macroscopic properties

At 20°C, perfect slip and mechanical twinning coexist and interact. In Figure 5(b), dislocation tangles are observed against twin boundaries, which act as obstacles to dislocation motion. Furthermore, mechanical twinning affects the strain hardening rate of the material as it gradually reduces the mean free path of dislocations in a sort of dynamic Hall-Petch effect [51,52]. This phenomenon continuously strengthens the material, even at high strains, which retards plastic instability and flow localization. In addition, mechanical twinning is a plastic deformation mechanism that contributes to the increase of the total tensile elongation. The formation of a mechanical twin

produces a minimum lattice translation equal to the magnitude of three partial Burgers vectors [53]. In contrast to dislocations, this displacement is definitive since twins are not subject to easy recombination or rearrangement. All these elements lead to increased elongation and strain hardening at 20°C.

At 200°C, mechanical twinning is suppressed and only dislocation glide is active. At this temperature, cross-slip is energetically favorable and allows dislocations to overcome defects without difficulty. Furthermore, cross-slip facilitates the recombination and the rearrangement of dislocations into cells (see Figure 5(c) and (d)). When this occurs, the strain hardening of the material quickly saturates, and the strain hardening rate decreases. Thus, the strain localizes and a neck forms, so the total elongation of the material is limited. Therefore, the suppression of twinning and the occurrence of cross-slip lead to reduced elongation and strain hardening at 200°C.

5 Conclusions

In this work, the singular loss of ductility in 15Cr15Ni-Ti AIM1 stainless steel at moderate temperature was investigated by a multi-scale characterization of the deformation mechanisms involving macroscopic and microscopic mechanical tests as well as mesoscopic and microscopic observations. The obtained results on mechanical properties, deformation landscapes and lattice defect characteristics lead to the following conclusions:

1. The analysis of the tensile tests shows that the uniform and total elongations drastically decrease for both solution-annealed and cold-worked conditions when the temperature increases from 20 to 200°C.

2. Post-mortem characterizations reveal the coexistence of perfect slip and mechanical twinning at 20°C, whereas only perfect slip associated with cross-slip is active at 200°C.
3. A continuous increase of the SFE is observed over the temperature range from 20 to 300°C. In particular, the measured values are 27 mJ/m² at 20°C and 46 mJ/m² at 200°C.
4. Mechanical twinning produces a high strain hardening of the microstructure by a dynamic Hall-Petch effect at 20°C, which greatly enhances the ductility. The extinction of twinning at 200°C results in reduced strain hardening and rapid flow localization and necking.
5. The evolution of the deformation mechanisms between 20 and 200°C is explained in terms of the energy required for competing mechanisms. At 20°C, the formation of a stacking fault requires reduced energy, while at 200°C dislocation cross slip is more energetically favorable.

6 Acknowledgments

This work partially pertains to the French Government program “Investissements d’Avenir” (LABEX INTERACTIFS, reference ANR-11-LABX-0017-01) and was partially supported by « Nouvelle Aquitaine » Region and by European Structural and Investment Funds (ERDF reference : P-2016-BAFE-94/95).

The authors acknowledge financial support from the CNRS-CEA “METSA” French network (FR CNRS 3507) on the plateform CEMES (Toulouse).

7 References

[1] P. Lacombe, B. Baroux, G. Béranger, L. Colombier, J. Hochmann, J.H. Davidson, J.B. Lindquist, Stainless steels, Les Editions de Physique, 1993.

[2] P. Marshall, Austenitic stainless steels: microstructure and mechanical properties, Springer Science & Business Media, 1984.

[3] P. Yvon, F. Carré, Structural materials challenges for advanced reactor systems, J. Nucl. Mater. 385 (2009) 217–222.

[4] S.J. Zinkle, G. Was, Materials challenges in nuclear energy, Acta Mater. 61 (2013) 735–758.

[5] T. Allen, H. Burlet, R.K. Nanstad, M. Samaras, S. Ukai, Advanced structural materials and cladding, MRS Bull. 34 (2009) 20–27.

[6] P. Yvon, M. Le Flem, C. Cabet, J.L. Seran, Structural materials for next generation nuclear systems: Challenges and the path forward, Nucl. Eng. Des. 294 (2015) 161–169.

[7] M. Le Flem, N. Devictor, G. Mignot, F. Varaine, C. Venard, L. Martin, M. Phelip, D. Lorenzo, F. Serre, F. Bertrand, others, Status of the French R&D on ASTRID core materials, in: Charlotte, USA, 2014.

[8] T. Beck, V. Blanc, J.-M. Escleine, D. Haubensack, M. Pelletier, M. Phelip, B. Perrin, C. Venard, Conceptual design of ASTRID fuel sub-assemblies, Nucl. Eng. Des. 315 (2017) 51–60. doi:10.1016/j.nucengdes.2017.02.027.

[9] M. Chenaud, N. Devictor, G. Mignot, F. Varaine, C. Venard, L. Martin, M. Phelip, D. Lorenzo, F. Serre, F. Bertrand, others, Status of the ASTRID core at the end of the pre-conceptual design phase 1, Nucl. Eng. Technol. 45 (2013) 721–730.

[10] L. Courtin, S. Urvoy, D. Bossu, S. Bosonnet, M. Tabarant, B. Kedjar, P. Olier, L. Thilly, Comparison of 15Cr-15Ni austenitic steel cladding tubes obtained by HPTR cold pilgering or by cold drawing, in: Key Eng. Mater., Trans Tech Publ, 2015: pp. 38–46.

[11] L. Courtin, Optimisation de la transformation à froid des tubes de gaine en acier austénitique 15-15TI AIM1, Université de Poitiers, 2015.

[12] D. Braski, P. Maziasz, Tensile properties of unirradiated PCA from room temperature to 700° C, J. Nucl. Mater. 122 (1984) 338–342.

[13] V.D. Vijayanand, K. Laha, P. Parameswaran, M. Nandagopal, S. Panneer Selvi, M.D. Mathew, Influence of thermo-mechanical treatment on the tensile properties of a modified 14Cr–15Ni stainless steel, J. Nucl. Mater. 453 (2014) 188–195. doi:10.1016/j.jnucmat.2014.06.067.

[14] M. Nandagopal, P. Parameswaran, V. Vijayanand, S. Panneerselvi, K. Laha, M. Mathew, Recrystalization Behavior of Coldworked 14Cr-15Ni-2Mo Austenitic Stainless Steel Under Tensile Deformation, High Temp. Mater. Process. 32 (2013) 413–420.

[15] J. Brnic, G. Turkalj, M. Canadija, D. Lanc, AISI 316Ti (1.4571) steel—Mechanical, creep and fracture properties versus temperature, J. Constr. Steel Res. 67 (2011) 1948–1952. doi:10.1016/j.jcsr.2011.06.011.

[16] T.S. Byun, N. Hashimoto, K. Farrell, Temperature dependence of strain hardening and plastic instability behaviors in austenitic stainless steels, Acta Mater. 52 (2004) 3889–3899. doi:10.1016/j.actamat.2004.05.003.

[17] H. Barman, A. Hamada, T. Sahu, B. Mahato, J. Talonen, S. Shee, P. Sahu, D. Porter, L. Karjalainen, A Stacking Fault Energy Perspective into the Uniaxial Tensile Deformation Behavior and Microstructure of a Cr-Mn Austenitic Steel, Metall. Mater. Trans. A. 45 (2014) 1937–1952.

[18] O. Grässel, L. Krüger, G. Frommeyer, L. Meyer, High strength Fe–Mn–(Al, Si) TRIP/TWIP steels development—properties—application, Int. J. Plast. 16 (2000) 1391–1409.

[19] O. Bouaziz, S. Allain, C.P. Scott, P. Cugy, D. Barbier, High manganese austenitic twinning induced plasticity steels: A review of the microstructure properties relationships, Curr. Opin. Solid State Mater. Sci. 15 (2011) 141–168. doi:10.1016/j.cossms.2011.04.002.
[20] B.C. De Cooman, Y. Estrin, S.K. Kim, Twinning-induced plasticity (TWIP) steels, Acta Mater. 142 (2018) 283–362. doi:10.1016/j.actamat.2017.06.046.
[21] S. Allain, J.-P. Chateau, O. Bouaziz, S. Migot, N. Guelton, Correlations between the calculated stacking fault energy and the plasticity mechanisms in Fe–Mn–C alloys, Mater. Sci. Eng. A. 387 (2004) 158–162.
[22] T.-H. Lee, E. Shin, C.-S. Oh, H.-Y. Ha, S.-J. Kim, Correlation between stacking fault energy and deformation microstructure in high-interstitial-alloyed austenitic steels, Acta Mater. 58 (2010) 3173–3186. doi:10.1016/j.actamat.2010.01.056.
[23] Byun, On the stress dependence of partial dislocation separation and deformation microstructure in austenitic stainless steels, Acta Mater. 51 (2003) 3063–3071.
[24] X. Wu, X. Pan, J.C. Mabon, M. Li, J.F. Stubbins, The role of deformation mechanisms in flow localization of 316L stainless steel, J. Nucl. Mater. 356 (2006) 70–77. doi:10.1016/j.jnucmat.2006.05.047.
[25] R.M. Langford, C. Clinton, In situ lift-out using a FIB-SEM system, Micron. 35 (2004) 607–611. doi:10.1016/j.micron.2004.03.002.
[26] A. Couret, J. Crestou, S. Farenc, G. Molenat, N. Clément, A. Coujou, D. Caillard, In situ deformation in TEM: recent developments, Microsc. Microanal. Microstruct. 4 (1993) 153–170.
[27] F. Mompiou, D. Caillard, M. Legros, Grain boundary shear–migration coupling—I. In situ TEM straining experiments in Al polycrystals, Acta Mater. 57 (2009) 2198–2209. doi:10.1016/j.actamat.2009.01.014.
[28] A. Ruff, Measurement of stacking fault energy from dislocation interactions, Metall. Mater. Trans. B. 1 (1970) 2391–2413.
[29] B. Mahato, T. Sahu, S.K. Shee, P. Sahu, T. Sawaguchi, J. Kömi, L.P. Karjalainen, Simultaneous twinning nucleation mechanisms in an Fe–Mn–Si–Al twinning induced plasticity steel, Acta Mater. 132 (2017) 264–275. doi:10.1016/j.actamat.2017.04.046.
[30] J. Lu, L. Hultman, E. Holmström, K.H. Antonsson, M. Grehk, W. Li, L. Vitos, A. Golpayegani, Stacking fault energies in austenitic stainless steels, Acta Mater. 111 (2016) 39–46.
[31] D.T. Pierce, J. Bentley, J.A. Jiménez, J.E. Wittig, Stacking fault energy measurements of Fe–Mn–Al–Si austenitic twinning-induced plasticity steels, Scr. Mater. 66 (2012) 753–756. doi:10.1016/j.scriptamat.2012.01.050.
[32] L. Rémy, A. Pineau, B. Thomas, Temperature dependence of stacking fault energy in close-packed metals and alloys, Mater. Sci. Eng. 36 (1978) 47–63.
[33] M. Whelan, Dislocation interactions in face-centred cubic metals, with particular reference to stainless steel, Proc R Soc Lond A. 249 (1959) 114–137.
[34] L.M. Brown, A.R. Thölén, Shape of three-fold extended nodes, Discuss Faraday Soc. 38 (1964) 35–41. doi:10.1039/DF9643800035.
[35] I. Databooks, Austenitic chromium-nickel stainless steels–engineering properties at elevated temperatures, Int. Nickel Co. (1968).
[36] T.C. Tisone, J.O. Brittain, M. Meshii, Stacking Faults in a Cu-15 at% Al Alloy. I. The Short Range Order and Temperature Dependence of the Stacking Fault Energy, Phys. Status Solidi B. 27 (1968) 185–194. doi:10.1002/pssb.19680270119.
[37] G. Meric de Bellefon, J.C. van Duysen, K. Sridharan, Composition-dependence of stacking fault energy in austenitic stainless steels through linear regression with random intercepts, J. Nucl. Mater. 492 (2017) 227–230. doi:10.1016/j.jnucmat.2017.05.037.

[38] J. Borges, A. Padilha, K. Imakuma, Determination of the stacking fault energies of face centured cubic metals and alloys by X-rays diffraction, Instituto de Pesquisas Energeticas e Nucleares, 1988.
[39] R. Latanision, A. Ruff, The temperature dependence of stacking fault energy in Fe-Cr-Ni alloys, Metall. Trans. 2 (1971) 505–509.
[40] F. Lecroisey, A. Pineau, Martensitic transformations induced by plastic deformation in the Fe-Ni-Cr-C system, Metall. Mater. Trans. B. 3 (1972) 391–400.
[41] F. Abrassart, Stress-induced γ→ α martensitic transformation in two carbon stainless steels. Application to trip steels, Metall. Trans. 4 (1973) 2205–2216.
[42] S. Hong, The tensile and low-cycle fatigue behavior of cold worked 316L stainless steel: influence of dynamic strain aging, Int. J. Fatigue. 26 (2004) 899–910. doi:10.1016/j.ijfatigue.2003.12.002.
[43] D. Michel, J. Moteff, A. Lovell, Substructure of type 316 stainless steel deformed in slow tension at temperatures between 21 and 816 C, Acta Metall. 21 (1973) 1269–1277.
[44] T.S. Byun, E.H. Lee, J.D. Hunn, Plastic deformation in 316LN stainless steel – characterization of deformation microstructures, J. Nucl. Mater. 321 (2003) 29–39. doi:10.1016/S0022-3115(03)00195-8.
[45] G. Meric de Bellefon, J.C. van Duysen, Tailoring plasticity of austenitic stainless steels for nuclear applications: Review of mechanisms controlling plasticity of austenitic steels below 400 °C, J. Nucl. Mater. 475 (2016) 168–191. doi:10.1016/j.jnucmat.2016.04.015.
[46] A. Dumay, J.-P. Chateau, S. Allain, S. Migot, O. Bouaziz, Influence of addition elements on the stacking-fault energy and mechanical properties of an austenitic Fe–Mn–C steel, Mater. Sci. Eng. A. 483–484 (2008) 184–187. doi:10.1016/j.msea.2006.12.170.
[47] K. Sato, M. Ichinose, Y. Hirotsu, Y. Inoue, Effects of deformation induced phase transformation and twinning on the mechanical properties of austenitic Fe–Mn–Al alloys, ISIJ Int. 29 (1989) 868–877.
[48] G. Frommeyer, U. Brüx, P. Neumann, Supra-Ductile and High-Strength Manganese-TRIP/TWIP Steels for High Energy Absorption Purposes., ISIJ Int. 43 (2003) 438–446. doi:10.2355/isijinternational.43.438.
[49] J. Kim, S.-J. Lee, B.C. De Cooman, Effect of Al on the stacking fault energy of Fe–18Mn–0.6C twinning-induced plasticity, Scr. Mater. 65 (2011) 363–366. doi:10.1016/j.scriptamat.2011.05.014.
[50] S. Allain, O. Bouaziz, J. Chateau, Proc int conf SHSS, in: Verona, Italia, 2010.
[51] O. Bouaziz, N. Guelton, Modelling of TWIP effect on work-hardening, Mater. Sci. Eng. A. 319–321 (2001) 246–249. doi:10.1016/S0921-5093(00)02019-0.
[52] S. Allain, J.-P. Chateau, O. Bouaziz, A physical model of the twinning-induced plasticity effect in a high manganese austenitic steel, Mater. Sci. Eng. A. 387–389 (2004) 143–147. doi:10.1016/j.msea.2004.01.060.
[53] S. Kibey, J.B. Liu, D.D. Johnson, H. Sehitoglu, Predicting twinning stress in fcc metals: Linking twin-energy pathways to twin nucleation, Acta Mater. 55 (2007) 6843–6851. doi:10.1016/j.actamat.2007.08.042.

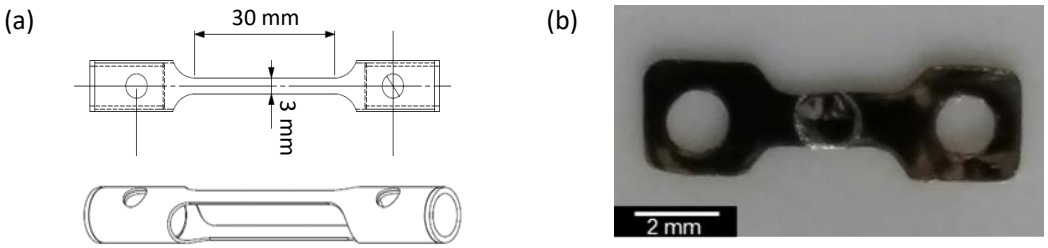

Figure 1 : (a) geometry of a two-leg macro-tensile specimen, (b) geometry of a micro-tensile specimen.

(2-column fitting image – color)

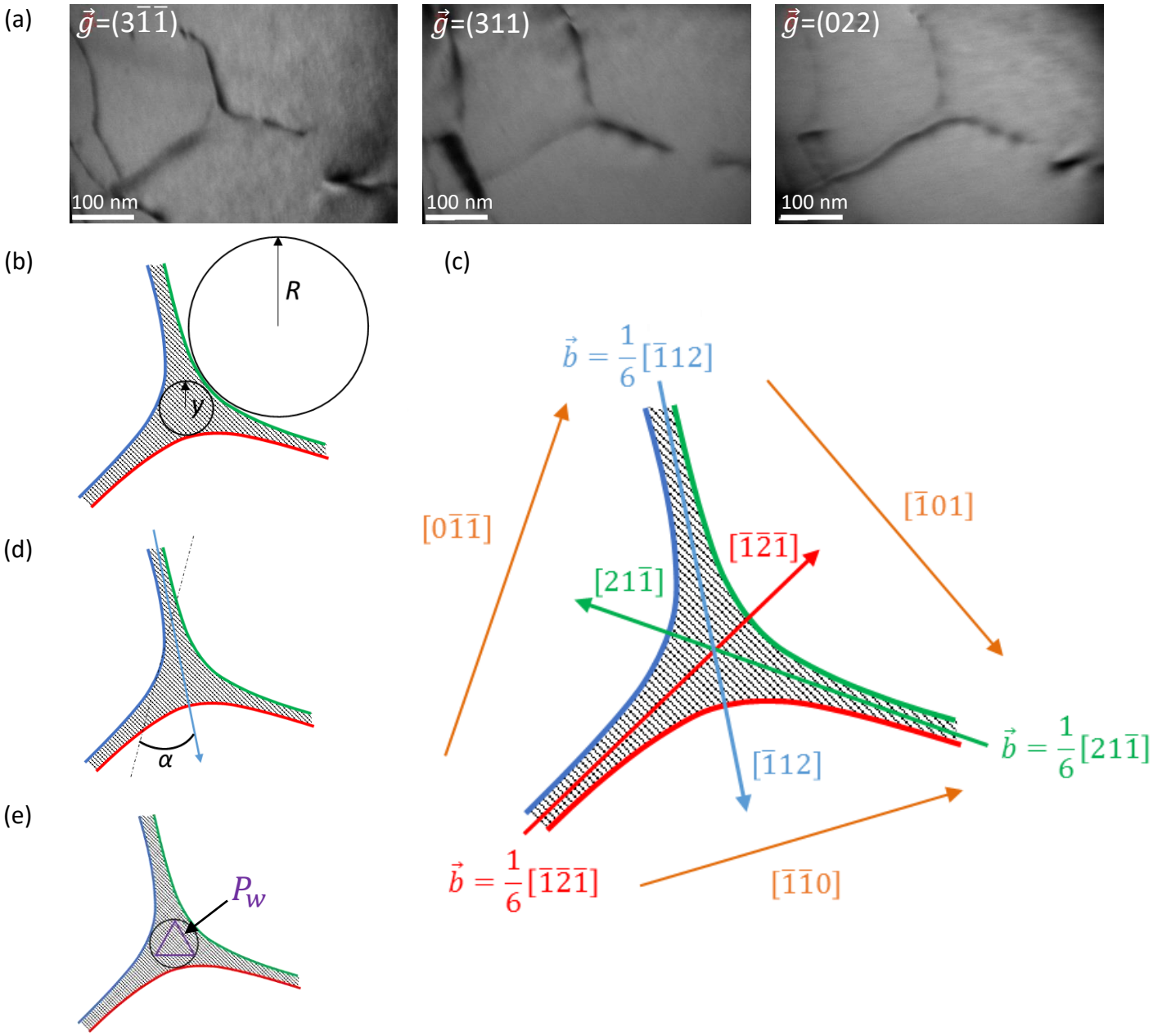

Figure 2: (a) Extended dislocation node under different observation conditions in S-SA at 20°C; (b) Measurement of y and R; (c) Characterization of the dislocations of the node; (d) Measurement of the angle α; (e) Description of the perimeter P_w .

(2-column fitting image – color)

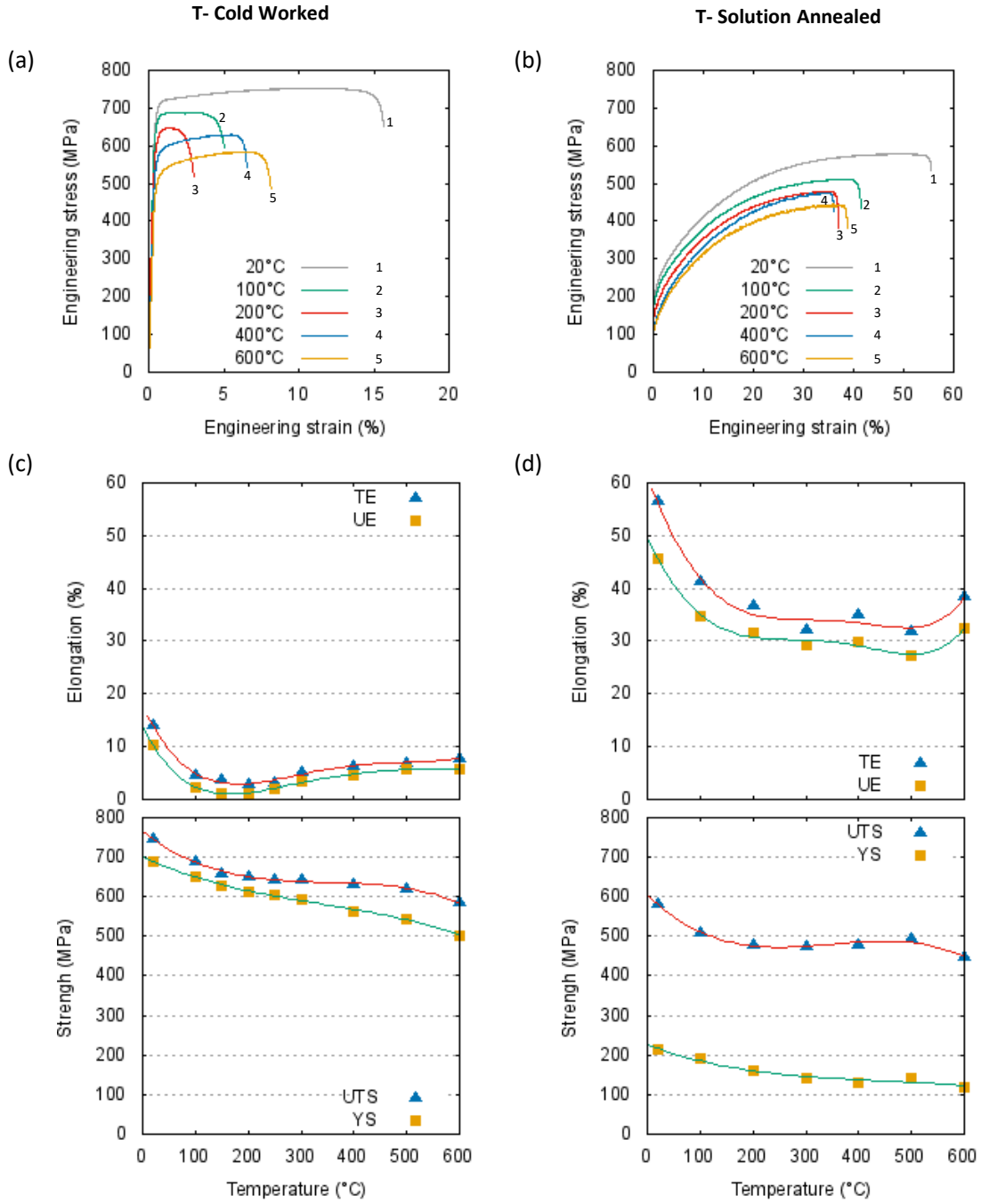

Figure 3: Temperature dependence of the engineering stress-strain curves for (a) T-CW, (b) T-SA, and temperature dependence of tensile properties (UE, TE, YS, UTS) for (c) T-CW, (d) T-SA.

(2-column fitting image – color)

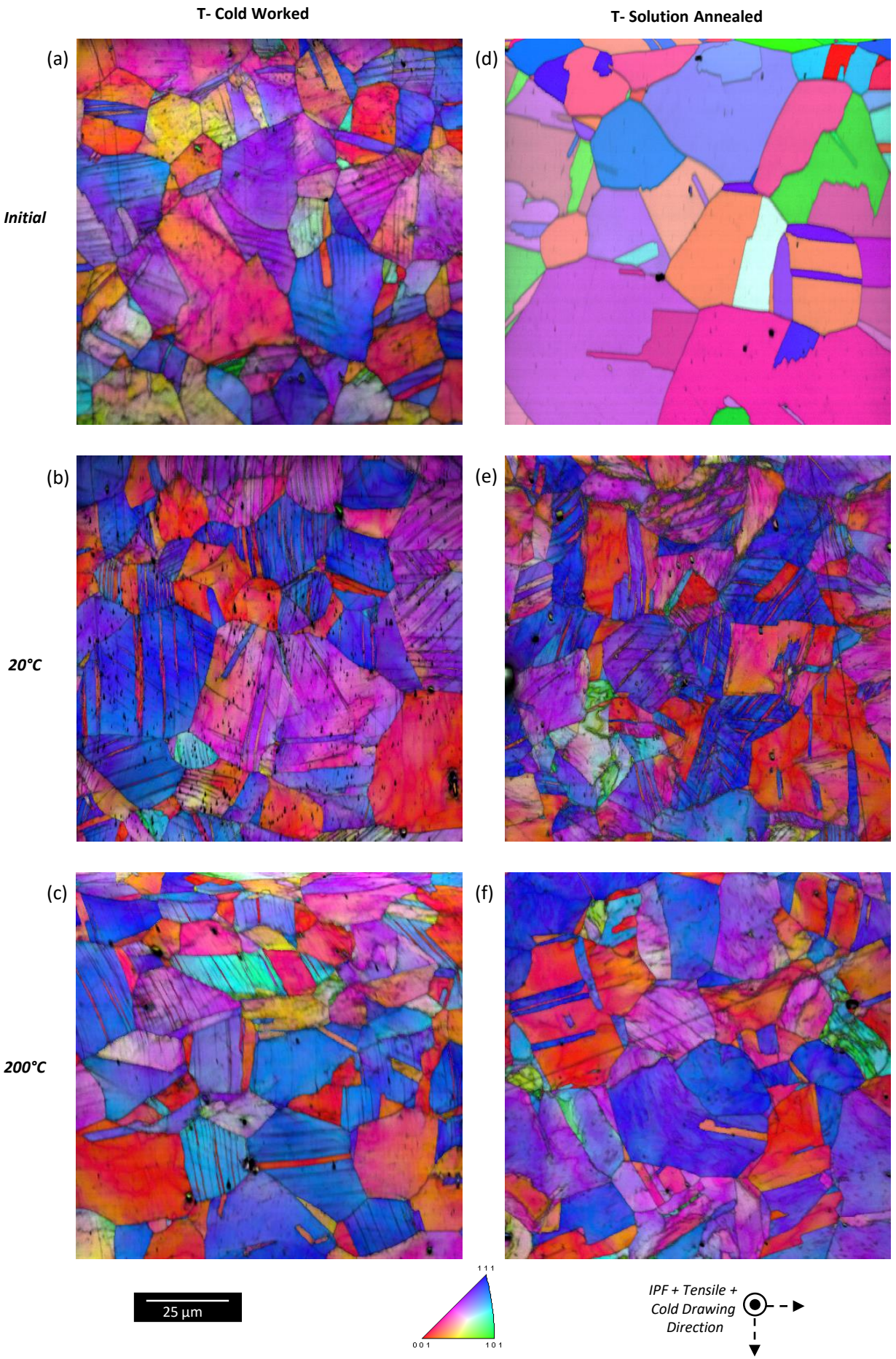

Figure 4: Inverse Pole Figure (IPF) and Image Quality (IQ): (a) Initial T-CW, (b) T-CW tensile-tested to UE at 20°C, (c) T-CW tensile-tested to UE at 200°C, (d) Initial T-SA, (e) T-SA tensile-tested to UE at 20°C, (f) T-SA tensile-tested to UE at 200°C.*

(2-column fitting image – color)

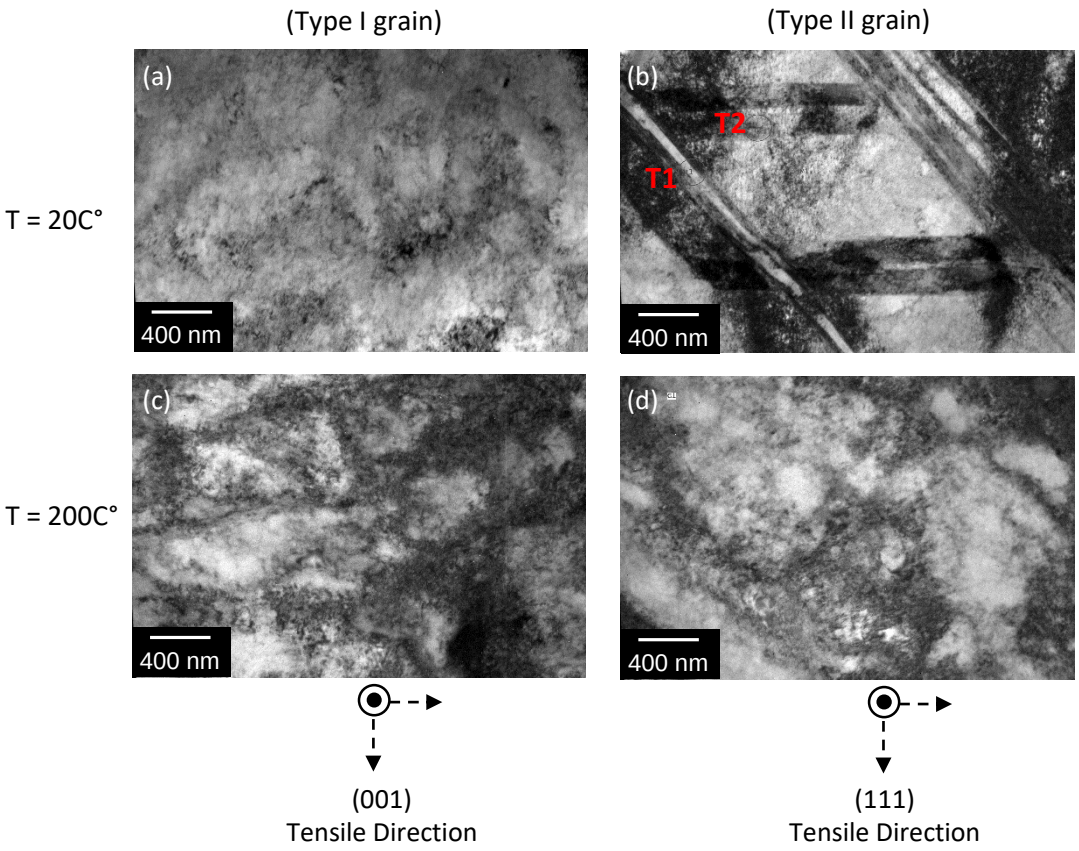

Figure 5: TEM images after FIB extraction: (a) from a type I grain on T-SA tensile-tested to UE at 20°C, (b) from a type II grain on T-SA tensile-tested to UE at 20°C, (c) from a type I grain on T-SA tensile-tested to UE at 200°C, (d) from a type II grain on T-SA tensile-tested to UE at 200°C.

(2-column fitting image – color)

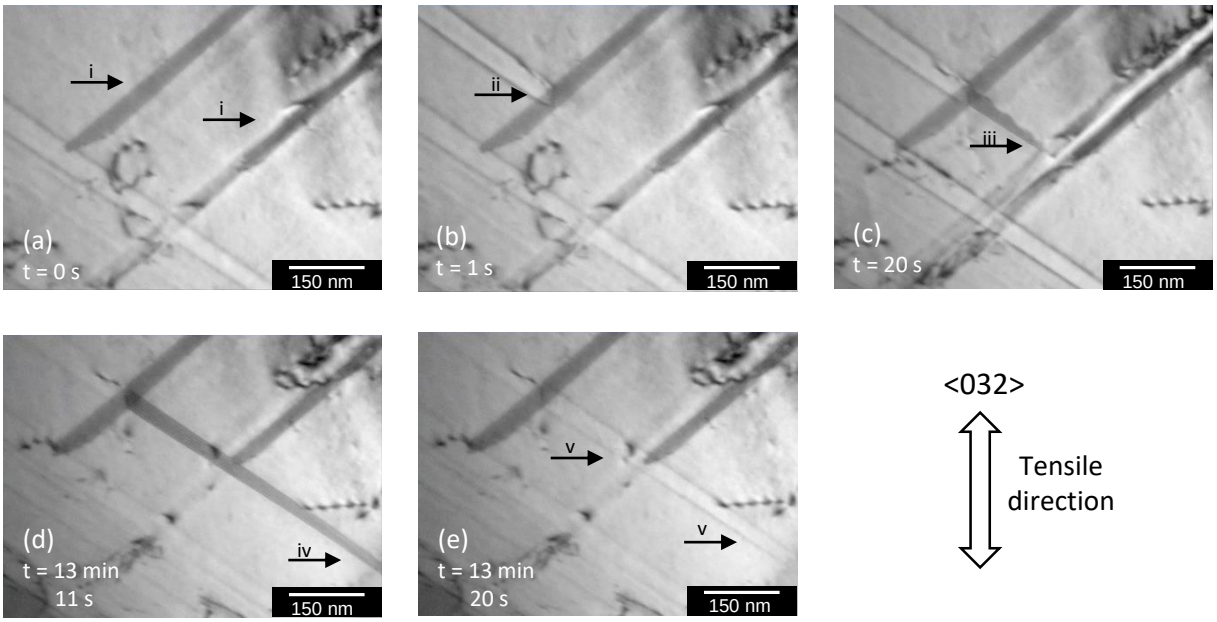

Figure 6: Video sequence showing the nucleation of a stacking fault at 20°C.

(2-column fitting image – no color)

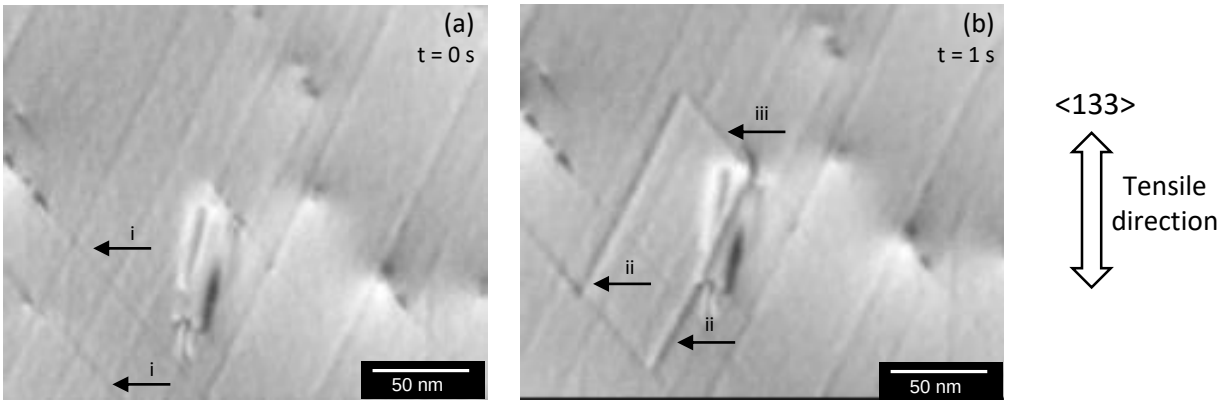

Figure 7: Video sequence of cross-slip at 200°C.

(2-column fitting image – no color)

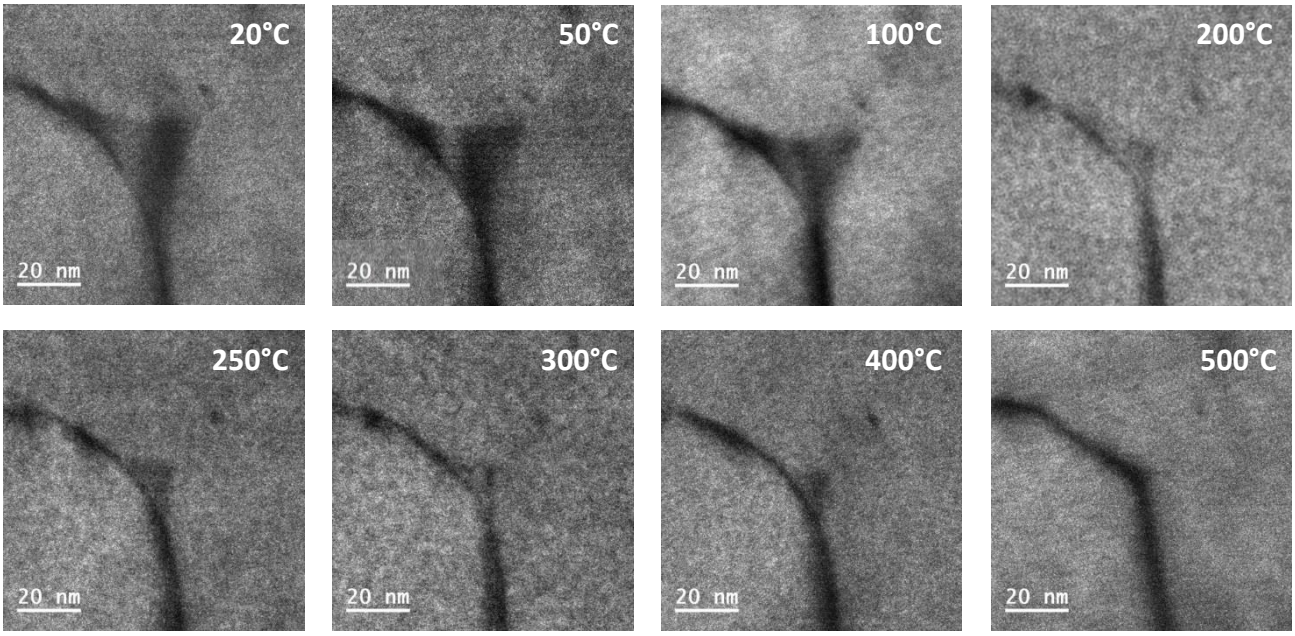

Figure 8: Evolution of the size of an extended dislocation node as function of temperature in S-SA.

(2-column fitting image – no color)

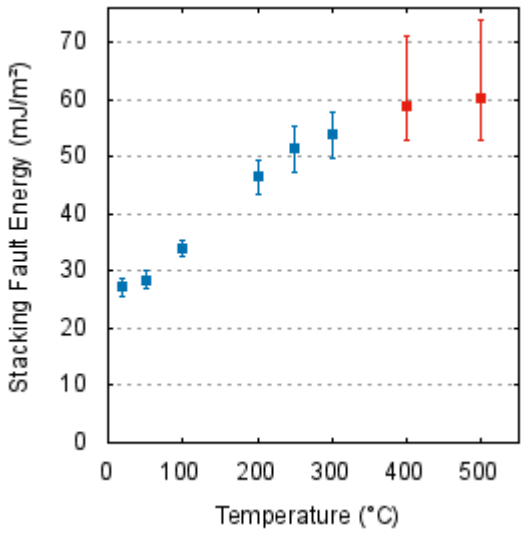

Figure 9: Calculated SFE values as a function of temperature (red dots have a higher uncertainty).

(single column fitting image – color)

Elements	Cr	Ni	Ti	C	Mo	Si	Mn	P	N
Weight (%)	14.3 ±0.7	14.7 ±0.6	0.40 ±0.08	0.091 ±0.001	1.51 ±0.12	0.84 ±0.05	1.42 ±0.09	0.04 ±0.01	0.006 ±0.001

Table 1: Main alloying elements of AIM1 (in wt. %).

T (°C)	μ (GPa)	υ	y (nm)	R (nm)	γ (mJ/m²)	$\Delta\gamma$ (mJ/m²)
20	80.3	0.28	16 (±0.5)	72 (±5)	27	± 1
50	77.8	0.28	15 (±0.5)	69 (±5)	28	±1
100	75.5	0.28	12 (±0.5)	55 (±5)	34	±2
200	73.6	0.29	8 (±0.5)	36 (±5)	46	±3
250	71.4	0.30	7 (±0.5)	33 (±5)	51	±4
300	69.2	0.33	6.5 (±0.5)	31 (±5)	53	±4
400	67.3	0.36	5.5 (±1)	27 (±10)	(59)	-6/+12
500	65.2	0.32	5 (±1)	22 (±10)	(60)	-7/+14

Table 2: Parameters and calculated SFE values as a function of temperature.